Tomographic Image Reconstruction in Experimental Fluid Dynamics: Synopsis and Problems

Stefania Petra*, Christoph Schnörr*, Andreas Schröder, Bernhard Wieneke§**

* "Ruprecht-Karls" University of Heidelberg, Germany; e-mail: {petra, schnoerr}@math.uni-heidelberg.de; the authors gratefully acknowledge financial support by the DFG Grant SCHN 457/10-1;
** German Aerospace Center (DLR) Göttingen, Germany; e-mail: andreas.schroeder@dlr.de;

§ LaVision GmbH, Göttingen, Germany; e-mail: bwieneke@lavision.de;

Abstract

Particle Image Velocimetry (PIV) denotes a prevailing technique for imaging turbulent fluids with high-speed cameras. Corresponding image sequences provide the basis for estimating such flows and related flow patterns through image processing. While so far this technique has been applied in two dimensions (2D) in terms of an illuminated plane intersecting the volume, recent research focuses on imaging fluids directly in 3D. This paper provides a synopsis of the state-of-the-art and its connections to previous research work on image restoration. We address the basic problems involved and point out promising research directions for reconstructing scalar-valued particle functions from few tomographical measurements. Solutions to these problems will provide an essential processing step prior to the estimation of 3D flows from reconstructed volume functions.

1 Introduction

Particle image velocimetry (PIV) is an optical method for measuring velocities of fluids [24]. For the purpose of visualization the fluid is seeded with particles that follow the flow dynamics. From the motion of these seeding particles the velocity information is obtained. For a recent overview of the history of PIV techniques, we refer to [1].

Among the different 3D velocimetry techniques presently available, *tomographic particle image reconstruction (TomoPIV)* [11] has recently received most attention, due to its increased seeding density in comparison to *3D particle tracking velocimetry (3D PTV)* [20], its relatively low costs and complexity of the necessary measurement apparatus in comparison to *holographic PIV* [15], and its capability of providing instantaneous flow field measurements irrespective of flow velocity, as opposed to *scanning PIV* [5]. TomoPIV is a novel

experimental technique, based on multiple camera-system, three-dimensional volume illumination and 3D reconstruction of seeding particles within the 3D measurement volume. The essential step of this technique is the 3D particle reconstruction as a light intensity distribution (3D image) by optical tomography. Thus it reduces to an 3D *image reconstruction from projections* problem, which can be formulated as an underdetermined system of linear equations of the form

$$Ax = b \ ,$$

as will be detailed in Section 2. Such systems, disregarding for the moment the inconsistent case, will have infinitely many solutions. An optimization criterium has to be specified, according to which a particular solution will be singled out from all those satisfying the measurements. The analysis of such a solution concept for the 3D particle image reconstruction problem is the main concern of the present work, focusing more on the adequate choice for the objective function within the optimization approach for accurate reconstruction, and less on algorithmic complexity and efficient runtimes.

In a subsequent step, provided that two subsequent 3D particle images have been obtained by means of a robust reconstruction algorithm, a *cross correlation technique* [25] returns an estimate of the instantaneous velocity field within the volume in focus.

The present paper is structured as follows. We begin our discussion with a description of the TomoPIV principle in Section 2. Next, we take a more detailed look at ART and MART, two of the most well-known *algebraic reconstruction techniques*. The algebraic reconstruction technique (ART) and the *multiplicative ART (MART)* appeared in [13] for use in computerized tomography (CT) scanning reconstruction. The ART algorithm produces a least-squares solution of minimal Euclidian norm. MART is a *maximum entropy* (ME) algorithm and defines the state-of-the-art of TomoPIV [11].

There are important differences, however, between tomographic medical imaging and particle image reconstruction. In medical imaging the observations are usually made at regular sample angles, and the image is oversampled. TomoPIV sampling, on the other hand, is undersampled to make the high-speed imaging process feasible, resulting in an ill-posed reconstruction problem. Moreover, ART and MART do not take advantage of the fact that the basic shape of the object to be reconstructed is known: a sparse distribution of small particles of equal size in a specified volume. It will turn out, mainly because of this characteristic, that ℓ_2-minimization is an inadequate optimization approach when applied to particle image reconstruction, since it provides a much to dense "solution". On the other hand, entropy

maximization seems to provide satisfactory results for sparse enough particle distributions. Increasing the seeding density, however, this approach will exhibit a behavior similar to ℓ_2-minimization. But higher particle densities are desirable since they ease subsequent flow estimation. Although the treatment of this paper is mainly theoretic, we will report some experimental results illustrating some basic points in Section 6.

2 Image Reconstruction within Tomo-PIV

The working principle of TomoPIV as described in [11] is schematically shown in Fig. 1. Seeding particles within the measurement volume are illuminated by a pulsed light source, and the scattered light pattern is recorded simultaneously from several viewing directions using CCD cameras. The 3D particle distribution (the object) is reconstructed as a 3D light intensity distribution from its projections (2D images) on the CCD arrays. The particle displacement (hence velocity) within the interrogation volume is then obtained by the 3D cross-correlation of the reconstructed particle distribution at the two exposures, similar to the approach in [25].

TomoPIV [11] adopts a simple discretization for an image-reconstruction problem known as the *algebraic image reconstruction* model [7], which assumes that the image consists of an array of unknowns (voxels), and sets up algebraic equations for the unknowns in terms of measured projection data. The latter are the pixel entries in the recorded 2D images.

We consider an alternative to the classical voxel discretization and assume that the image I to be reconstructed can be approximated by a linear combination of Gaussian-type *basis functions* $\mathcal{B}_j$,

$$I(z) \approx \sum_{j=1}^{n} x_j \mathcal{B}_j(z), \quad \forall z \in \Omega \subset \mathbb{R}^3\,, \quad \text{of the form} \tag{1}$$

$$\mathcal{B}_j(z) = e^{-\frac{\|z-p_j\|_2^2}{2\sigma^2}}, \quad \text{for } z \in \mathbb{R}^3 : \|z-p_j\|_2 \le r\,, \tag{2}$$

or value 0, if $\|z-p_j\|_2 > r$, located at a Cartesian equidistant 3D grid $p_j\,,\ j = 1,\ldots,n$ within the volume of interest Ω. The choice of a Gaussian-type basis function is justified in the TomoPIV setting, since a particle projection in all directions results in a so-called *diffraction spot* of approximately 3 pixel diameter, compare Fig. 2. Based on geometrical optics, the recorded pixel intensity is the object intensity integrated along the corresponding line of

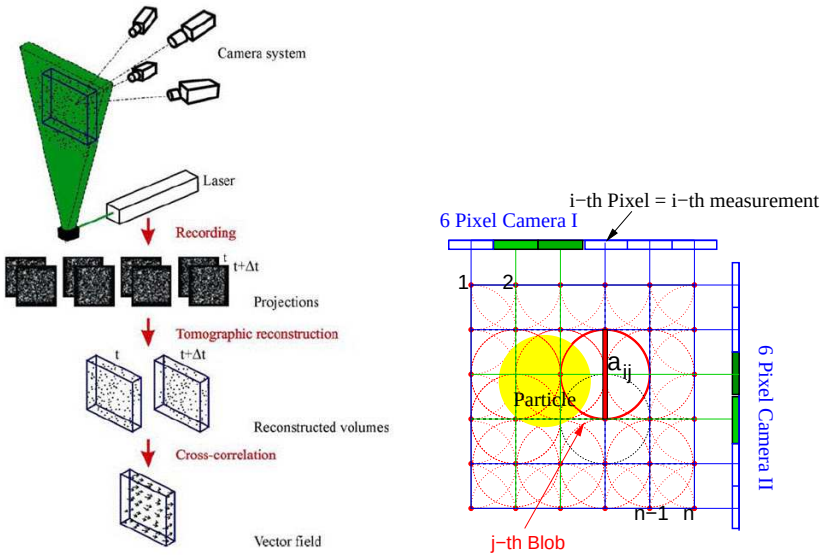

(a) TomoPIV principle (b) 2D sketch

Figure 1. (a) TomoPIV principle. (b) Discretization of an 2D volume and corresponding rays for two orthogonal projections

sight, obtained from a calibration procedure. Thus, the i-th measurement obeys

$$b_i :\approx \int_{L_i} I(z)dz \approx \sum_{j=1}^{n} x_j \int_{L_i} \mathcal{B}_j(z)dz = \sum_{j=1}^{n} x_j a_{ij}\,, \tag{3}$$

where a_{ij} is the value of the i-th pixel if the object to be reconstructed is the j-th basis function. The main task is to estimate the weights x_j from the recorded 2D images, corresponding to basis functions and solve

$$Ax \approx b\ . \tag{4}$$

We encounter limited-data problems since it is impossible to acquire integral data from the object at all angles at reasonable costs, due to the high speed of the measurement process. Thus the 3D image reconstruction problem is not straightforward since a single set of projections can result from many different 3D objects. But knowing roughly what the reconstructed object looks like can greatly improve reconstruction accuracy. The determination of the most likely 3D particle distribution will be discussed in the following sections, concentrating on two classical approaches.

3 Solution Concepts and Problem Characteristics

The approximation (4) reflects possible errors in modeling and measurement. Thus, a exact solution of the linear system

$$Ax = b \tag{5}$$

even if it would exist, and if we could compute it accurately, is not more desirable with respect to the underlying reconstruction problem, than some other, differently defined, "solution". The equations $a_{i*}^T x = b_i, i = 1, \ldots, m$, in (5) should be used in a way that reflects our confidence in the data. A classical approach, also known as *feasibility approach* [7], is to allow a deviation of Ax from the data b, solving for

$$b_i - \varepsilon_i \leq a_{i*}^T x \leq b_i + \varepsilon_i, \quad i = 1, \ldots, m, \tag{6}$$

where $\varepsilon_i > 0, i = 1, \ldots, m$, are some user specified tolerances. The above linear system of inequalities results in a *linear interval feasibility problem* [7]. It tries to find a solution within the neighborhoods of all hyperplanes $H_i := \{x \mid a_{i*}^T x = b_i\}, i = 1, \ldots, m$, rather than an intersection point as problem (5).

However, by the above relaxation approach the feasible set of (6) will be enlarged, and an additional criterion has to be applied to single out a unique solution of (6).

Additional information about the real-world problem provides additional inequalities that further restrict the feasible set both in (5) and (6). A common idea in image reconstruction is to look for solutions satisfying $x \geq 0$. Note that negative weights x_j may give by (1) a negative intensity distribution I around p_j.

Throughout the rest of this paper, we make the somehow restrictive assumption that there is no noise corruption of the data, no measurement inaccuracies and no discretization errors. Thus we concentrate on ill-posedness of (5) in the sequel and report the investigation of the relaxed model (6) elsewhere.

Let us consider some special features of the system in (5). We have to handle a underdetermined system with $m << n$, having very sparse coefficient matrix $A \in \mathbb{R}^{m \times n}$, in general not of full rank. The sparsity structure of A is due to the fact that only a few basis function are on the line of sight of each particular camera pixel. By the nature of the problem, given the construction of the projection matrix A and the fact that the measured data represent intensities, we always have $a_{ij} \geq 0$ and $b_i \geq 0, \forall i = 1, \ldots, m, \forall j = 1, \ldots, n$. Often we encounter even zero measurements b_i, compare Fig. 2.

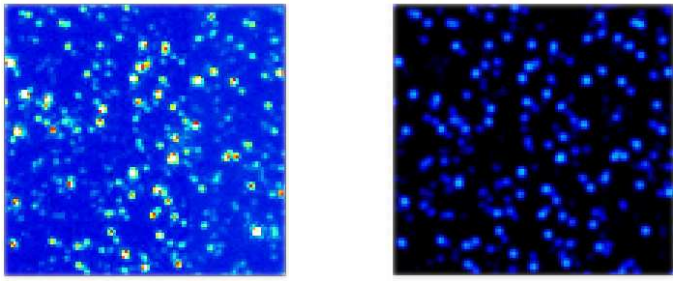

Figure 2. Typical projection (2D image) of a 3D particle distribution (3D image) before (left) and after (right) preprocessing

As a consequence, it is reasonable to remove equations with zero right-hand side. This will lead to a feasible set of reduced dimensionality as detailed next. Consider the feasible polyhedral set with respect to A and b

$$\mathcal{F} := \{x \mid Ax = b, x \geq 0\} \tag{7}$$

and let us introduce the following partitions of the index sets $I := \{1, \ldots, m\}$ and $J := \{1, \ldots, n\}$:

$$\begin{aligned} I_0 &:= \{i \in I \mid b_i = 0\} && \text{and} && \bar{I}_0 := I \setminus I_0, \\ J_0 &:= \{j \in J \mid \exists i \in I_0 : a_{ij} > 0\} && \text{and} && \bar{J}_0 := J \setminus J_0. \end{aligned}$$

Further define

$$\mathcal{F}_{red} := \{x \mid A_{\bar{I}_0 \bar{J}_0} x = b_{\bar{I}_0}, x \geq 0\}. \tag{8}$$

Then the following holds:

Proposition 1 *Let $A \in \mathbb{R}^{m \times n}, b \in \mathbb{R}^m$ have all nonnegative entries and $\mathcal{F}$ and $\mathcal{F}_{red}$ defined as in* (7) *and* (8) *respectively. Then*

$$\mathcal{F} = \{x \in \mathbb{R}^n \mid x_{J_0} = 0 \text{ and } x_{\bar{J}_0} \in \mathcal{F}_{red}\}. \tag{9}$$

Proof. Let $S := \{x \in \mathbb{R}^n \mid x_{J_0} = 0 \text{ and } x_{\bar{J}_0} \in \mathcal{F}_{red}\}$. We first show $S \subseteq \mathcal{F}$. Let $x \in S$. From this $x \geq 0$ follows directly. We just have to show $\sum_{j=1}^{n} a_{ij} x_j = b_i, \forall i \in I$. Indeed, for

$$i \in \bar{I}_0 : \quad \sum_{j=1}^{n} a_{ij} x_j = \sum_{j \in \bar{J}_0} \underbrace{a_{ij} x_j}_{=b_i} + \sum_{j \in J_0} a_{ij} \underbrace{x_j}_{=0} = b_i \ ,$$

whereas for

$$i \in I_0 : \quad \sum_{j=1}^{n} a_{ij} x_j = \sum_{j \in \bar{J}_0} \underbrace{a_{ij}}_{=0} x_j + \sum_{j \in J_0} \underbrace{a_{ij}}_{>a_{ij}} \underbrace{x_j}_{=0} = 0 = b_i \ .$$

Now let $x \in \mathcal{F}$ and consider any $i \in I_0$. Then

$$0 = b_i = \sum_{j=1}^{n} a_{ij} x_j = \sum_{j \in \bar{J}_0} \underbrace{a_{ij}}_{=0} x_j + \sum_{j \in J_0} \underbrace{a_{ij}}_{>a_{ij}} x_j \tag{10}$$

holds. Since $x \geq 0$, we obtain from (10) that $x_j = 0, \forall j \in J_0$. To show that $A_{\bar{I}_0 \bar{J}_0} x_{\bar{J}_0} = b_{\bar{I}_0}$, consider

$$i \in \bar{I}_0 : \quad \sum_{j \in \bar{J}_0} a_{ij} x_j = \sum_{j \in \bar{J}_0} a_{ij} x_j + \sum_{j \in J_0} a_{ij} \underbrace{x_j}_{=0} = \sum_{j=1}^{n} a_{ij} x_j = b_i \ .$$

Hence, $x_{J_0} = 0$ and $x_{\bar{J}_0} \in \mathcal{F}_{red}$. Thus $x \in S$. □

Remark 1 *The linear system* (5) *may have no (nonnegative) solution, infinitely many (nonnegative) solutions or exactly one nonnegative solution. According to [9] the latter case occurs when there is a sufficiently sparse solution to* (5)*.*

However, the common case is an infinite feasible set. Along with the feasibility approach, the *optimization approach* has prevailed in image reconstruction from limited data. Using this approach, also known as *regularization approach*, one has to specify an objective function $f : \mathbb{R}^n \to \mathbb{R}$, according to which a particular element of (5) or (7) is selected as solution to the original real-world problem.

Optimizing a (convex) function f with respect to linear constraints can be handled by a variety of optimization methods. But a general-purpose method can emerge as impracticable, since in particle image reconstruction there are millions of voxels resp. basis function in the 3D image and thousands of measurements m, resulting in matrices A that may be much too big to be stored in computer memory.

A common and successful class of algorithms used in image reconstruction from projections are row-action methods [7]. These iterative algorithms do not change the original matrix A, do not perform operations on the matrix as a

whole, but require only a single row of the matrix in each step of the and only need the predecessor x^k in order to compute x^{k+1}. As a consequence there is no need to store the entire matrix A in the computer's memory. Thus row-action methods are able to handle huge problem sizes. Furthermore, they are well suited for parallel computation.

4 Minimum Energy Solution with ART

In this and the following section we investigate two classical optimization approaches. Most commonly used is the ℓ_2-norm regularization, also called *minimum energy* approach:

$$(P_{LS}) \qquad \min \frac{1}{2}\|x\|_2^2 \ \texttt{s.t.}\ Ax = b \ , \tag{11}$$

The continuous differentiable and strictly convex objective function $f_{LS} := \frac{1}{2}\|x\|_2^2$ selects a unique solution of every instance of consistent equations (5). A further advantage of the minimum energy approach is the existence of a closed form solution $x^* = A^+ b$ to (11), involving the Moore-Penrose pseudo-inverse A^+. However, computing A^+ is not recommended in practical situations. Besides being error-prone, such a computation results in a dense matrix A^+. As a consequence the solution is typically nonzero in every component. Hence, solving for (11) is the wrong principle for our application. Yet, (11) together with its relaxation (6) is computationally tractable. A common and successful class of iterative algorithms, known as algebraic reconstruction techniques, exist to solve these problems.

ART was first published in [13] in connection with image reconstruction and was later recognised to be identical to Kaczmarz's algorithm [17] for solving the linear system (5). ART belongs to the class of row action methods. The iteration proceeds as follows:

Algorithm 1 *(Algebraic Reconstruction Technique (ART) - with relaxation and cyclic control)*

(S.0) Set $x^0 := 0$ *and* $k := 0$.

(S.1) Set $i := (k \mod m) + 1$ *and*

$$x_j^{k+1} = x_j^k + \lambda_k \frac{b_i - a_{i*}^T x^k}{\|a_{i*}\|^2} a_{ij}, \quad j = 1, \ldots, n \ , \tag{12}$$

where $\lambda_k \in (0, 2)$ *is a user specified parameter.*

(S.2) If $Ax^{k+1} = b$ is satisfied within the tolerance level: STOP.
Otherwise, increase the iteration counter $k \leftarrow k + 1$ and continue with (S.1).

For the above algorithm, we have in the consistent case the following convergence result:

Theorem 1 *[16] Assume that a solution to $Ax = b$ exists. For the all-zero starting vector x^0 and for $\lambda_k \in (0, 2)$, any sequence $\{x^k\}$ generated by Algorithm 1 converges to the unique optimum of problem (11), i.e. $x^*_{LS} = A^+b$.*

ART is a simple, intuitive algorithm. If the current guess x^k is too large, then the residual $b_i - a_{i*}^T x^k$, will be negative and decrease the value of the pixel. ART is a particular *Projection Onto Convex Sets (POCS)* algorithm [2], where the iterations project the current iterate on the hyperplanes defined by the rows of A and observations b. ART can be also viewed as a special instance of *Bregman's balancing method* [4], which for each $i := (k \mod m)+1$ finds

$$x^{k+1} = x^k + \lambda_k(P_{H_i}(x^k) - x^k) \ ,$$

where $P_{H_i}(x^k)$ is the orthogonal projection of x^k on the i-th hyperplane H_i.

This sequential POCS method converges in the consistent case to a point in the intersection of the convex sets, see [14, Th. 1]. However, in the inconsistent case it does not converge, but convergence of the cyclic subsequences, called *cyclic convergence*, can be shown [14, Th. 2].

For ART without relaxation, Kaczmarz [17] proved convergence to the unique solution of the system, provided A is square and invertible. Herman et al. showed in [16] that ART with relaxation converges in the consistent case. The case in which no solution exists has been considered by Tanabe [26], who proved convergence to a limit cycle of vectors. If, the relaxation parameter λ_k goes to zero, the element of the limit cycle approach the same vector. This has been considered by Censor et al. [6], who show that the limiting single vector is the least squares solution that is unique provided A has full rank. A different approach was adopted by Popa et al. in [23], where a Kaczmarz-type algorithm, called *Kaczmarz Extended with Relaxation Parameters (KERP)*, employs a modified right-hand side vector b to deal with the inconsistent case. Convergence of KERP towards a least-squares solution, irrespective of a starting point x^0, was proved in [22].

However, the least-squares solution may not be positive, even in the case of only positive entries in A and b. ART can be adapted to involve nonnegativity constraints by including certain constraining strategies [18] in the iterative

process, e.g. orthogonal projection of the current iterate after a full cycle on the positive orthant.

5 Maximum Entropy Solution with MART

Entropy has it's origin in information theory and can be defined as a measure of probabilistic uncertainty [8]. Entropy optimization has been applied to a wide range of practical problems, varying from transportation and location problems to speech recognition and image reconstruction. We refer to [12] for an overview on entropy optimization and its application in various fields. In this paper, we consider a finite-dimensional linearly constrained entropy-like problem

$$(P_E) \qquad \min \sum_{j=1}^{n} x_j \log(x_j) \quad \text{s.t.} \quad Ax = b, x \geq 0 \ , \tag{13}$$

in accordance to models used for image reconstruction [13, 7], where $E(x) := -f_E(x) := -\sum_{j=1}^{n} x_j \log(x_j)$ is the Boltzmann-Shannon entropy measure. We stress that x must be a probability distribution to properly form an entropy measure. So its interpretation in (13) as entropy is made only by analogy. Entropy maximization has been established in the field of tomographic PIV in [11].

Adding the constraint $x \geq 0$ is not only reasonable, but is also necessary for the maximum entropy approach, since the log function is defined only for positive values. Taking in account that $\lim_{t \searrow 0} t \log(t) = 0$, we define $0 \log 0 := 0$ and continuously extend f_E. Under our assumption that the feasible set $\mathcal{F} \neq \emptyset$, we can verify [3, Prop. A.8] that problem (P_E) has a global solution, since f_E is continuous and coercive.

Further notice that the objective function f_E of (P_E) is strictly convex over $\mathbb{R}^n_+$, since its Hessian is positive definite on $\mathbb{R}^n_{++}$. Hence (P_E) has a unique optimal solution. Moreover, if the set

$$\mathcal{F}_+ = \{x \in \mathbb{R}^n \mid Ax = b, x > 0\} \tag{14}$$

is nonempty, then the unique optimal solution is strictly positive. However, in view of Proposition 1, $\mathcal{F}_+ = \emptyset$ whenever $I_0 \neq \emptyset$. Such an assumption will therefore be inappropriate in our context. But since we are interested in analyzing methods (e.g. MART) for solving (P_E), which in general seek this strictly positive feasible solution, we will consider the reduced problem

$$\min_{x \in \mathcal{F}_{red}} \sum_{j \in \bar{J}} x_j \log(x_j), \tag{15}$$

under the assumption that $\mathcal{F}_{red} \neq \emptyset$. We stress that problem (15) is equivalent to (P_E) in the sense that a solution to the reduced problem (15) can be padded by zeros for all $j \in J_0$, see Proposition 1. For convenience, we will further refer to $A_{\bar{I}_0\bar{J}_0}$ and $b_{\bar{I}_0}$ by A and b and re-index $\bar{I}_0$ and $\bar{J}_0$ by $\{1,\ldots,m_r\}$ and $\{1,\ldots,n_r\}$ to simplify notation throughout this section.

Assuming $(\mathcal{F}_{red})_+ \neq \emptyset$, the strong duality theorem [3, Prop. 5.3.1] tells us that a necessary and sufficient condition for $x^* \in \mathbb{R}^{n_r}$ to be the positive optimal solution of problem (15), is the existence of $u^* \in \mathbb{R}_{m_r}$ such that

$$\begin{cases} x^* = e^{A^T u^* - \mathbf{1}}, \\ Ax^* = b \end{cases} \tag{16}$$

hold. Moreover, if u^* is a global optimum of the unconstrained dual problem

$$(D_E) \quad \max_{u \in \mathbb{R}^{m_r}} -\mathbf{1}^T e^{A^T u - \mathbf{1}} + b^T u, \tag{17}$$

there is no duality gap, i.e. $x^* \log(x^*) = -\mathbf{1}^T e^{A^T u^* - \mathbf{1}} + b^T u^*$. If $A = A_{\bar{I}_0\bar{J}_0}$ is a full rank matrix, the dual optimal solution u^* is unique. For a detailed development of this statement in a more general context, see [12, Th. 5.6].

Conditions (16), which are the K.K.T. conditions for the reduced entropy problem (15), and the dual problem (D_E) are the basis for developing solution methods to (15). We refer the reader to [12] for an overview over linearly constrained entropy problems.

The Multiplicative Algebraic Reconstruction Technique (MART) was first proposed in [13] is a row-action method analogous to ART. It applies only to systems in which $b > 0$ and A has only nonnegative entries. We ensure this by reducing the entropy maximization problem according to (9).

Algorithm 2 *(Multiplicative Algebraic Reconstruction Technique (MART) - with relaxation and cyclic control)*

(S.0) Choose $x^0 = e^{-\mathbf{1}}$ *and set* $k := 0$.

(S.1) Set $i := (k \mod m) + 1$ *and*

$$x_j^{k+1} = x_j^k \left(\frac{b_i}{a_{i*}^T x^k} \right)^{\mu_k a_{ij}}, \quad j = 1,\ldots,n\,, \tag{18}$$

where $\mu^k \in (0,1]$ *is a user specified relaxation parameter.*

(S.2) If $Ax^{k+1} = b$ is satisfied within the tolerance level: STOP.
Otherwise, increase the iteration counter $k \leftarrow k+1$ and continue with (S.1).

Censor et al. [19] showed the convergence of MART within the primal-dual framework even in the case of an *almost cyclic* control sequence [19], providing the starting vector x^0 is constant.

Theorem 2 *[19, Th. 18] Assume that $\mathcal{F}_{red} \neq \emptyset$, matrix A has only nonnegative entries and $Ax = b$ has been scaled so that $a_{ij} \leq 1$ for all $i \in \bar{I}_0$ and all $j \in \bar{J}_0$. Choose for all iterations k the relaxation parameter $\mu_k \in (0, 1]$. Then any sequence $\{x^k\}$ generated by Algorithm 2 converges to the unique optimum of problem* (15)*. Moreover, if the relative interior of $\mathcal{F}_{red} \neq \emptyset$, MART exhibits a linear convergence rate towards the unique (positive) solution.*

The linear rate of convergence was shown by Elfving [10]. If the set $(\mathcal{F}_{red})_+ = \emptyset$ the algorithm can converge sublinearly, see Section 6. The last two assumptions in Theorem 2 are not restrictive at all. The entries positivity assumption holds by the nature of the problem, whereas the normalization assumption is also easy to satisfy. We can further assume that the problem has been scaled so that the column sums of A are all equal to one. This amounts to redefine A and x by dividing a_{ij} by the sum of the j-th column and multiplying x_j by the same sum.

It turns out that besides the theoretical reasoning based on maximizing the dual in (17), MART has a geometrical interpretation similar to ART. The new iterate x^{k+1} is an approximation to the Bregman projection of x^k on the hyperplanes H_i. Indeed, f_E is a *Bregman function* [7, Lem. 2.1.3] and its associated *generalized distance* is the *Kullback-Leibner distance* between nonnegative vectors, i.e.

$$KL(x, y) := \sum_{j=1}^{n} \left(x_j \log \left(\frac{x_j}{y_j} \right) + y_j - x_i \right).$$

Thus x^{k+1} is an approximation to the minimizer of $KL(x, x^k)$ subject to H_i.

Recall that, following Censor [7], the Bregman projection with respect to a Bregman function f of a point x onto the closed convex set $\mathcal{X} \subseteq \mathbb{R}^n$ is the (necessarily unique) minimizer over $\mathcal{X}$, denoted $P^f_{\mathcal{X}}(x)$, of the functional $D_f(\cdot, x) : \mathbb{R}^n{}_{++} \to \mathbb{R}_+$, called generalized or Bregman distance, and defined by

$$D_f(y, x) = f(y) - f(x) - \nabla f(x)^T (y - x), \quad \forall y > 0,$$

i.e.

$$P_{\mathcal{X}}^{f}(x) = \text{argmin}_{y\in\mathcal{X}}\, D_f(y,x)\,.$$

Lemma 2.1.2 in [7] ensures that $P_{\mathcal{X}}^{f}(x)$ exists.

We conclude by pointing out that the behavior of MART in the case of inconsistent equations, that typically arise in real applications, is not known. In contrast, the behavior of ART when applied to inconsistent systems is well understood as discussed above.

6 Some Experiments and Discussion

We demonstrate the feasibility and the typical behavior of the approaches presented in Section 4 and 5 with two examples of small and medium size. The first is an illustrative example based on the the geometry presented in Figure 3(a). Three basis functions of the form

$$\mathcal{B}_j(z) = \begin{cases} 1, & \text{if } \|z-p_j\|_2 \le \frac{1}{2}, \\ 0, & \text{if } \|z-p_j\|_2 > \frac{1}{2}, \end{cases}$$

where $z \in \mathbb{R}^3$, are centred at each vertex $p_j, j = 1,2,3$, of an equilateral triangle of side $\frac{1}{2}$. Two 1-pixel cameras placed at infinity keep the scene in focus. The two lines of sight are $\overline{p_1p_2}$ and $\overline{p_1p_3}$ respectively, and intersect two basis functions each.

The resulting projection matrix is

$$A = \begin{pmatrix} 1 & 1 & \frac{1}{2} \\ 1 & \frac{1}{2} & 1 \end{pmatrix} \quad \text{and} \quad A^{+} = \begin{pmatrix} \frac{4}{17} & \frac{20}{17} & \frac{-14}{17} \\ \frac{4}{17} & \frac{14}{17} & \frac{20}{17} \end{pmatrix}^{T},$$

where A^+ denotes the Moore-Penrose inverse of A. Now suppose that a particle is positioned at p_1. In this case we "measure" the data $b = (1,1)^T$, according to (3).

The minimum energy solution of (11), which will be denoted by x_{LS}^* throughout this section, can be computed exactly

$$x_{LS}^* = A^+ b \approx (0.470588, 0.352941, 0.352941)^T\ .$$

The maximum energy solution of (13) can be computed exploiting the relations between the primal problem (P_E) and its dual (D_E). We obtained the unique global maximum $u^* := (u_1^*, u_2^*)$ of the dual objective in (17), where

$$u_1^* := \log\left(\frac{9}{16} + \frac{1}{2}\sqrt{b} - \frac{1}{2}\sqrt{\frac{81}{32} - \frac{1}{6a} + \frac{8e}{3} - \frac{32ae^2}{3} + \frac{\frac{729}{64} + 18e}{4\sqrt{b}}}\right),$$

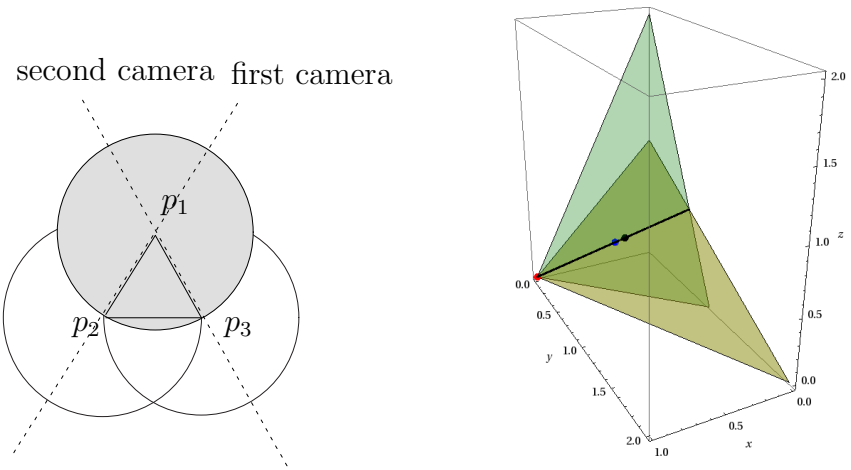

(a) First case (b) First case

Figure 3. (a) Discretization of a particle image and corresponding ray geometry. (b) Feasible set by restricting the intersection of two hyperplanes to the positive cone, together with the sparsest, the minimal ℓ_2-norm and the maximum entropy solution, from left to right.

$a := \frac{\left(\frac{2}{e}\right)^{2/3}}{\left(2048e+27\left(81+\sqrt{6561+12288e}\right)\right)^{1/3}}$, $b = \frac{81}{64} + \frac{1}{6a} + \frac{4e}{3} + \frac{32ae^2}{3}$ and $u_2^* := u_1^*$, using Mathematica. Indeed, performing some exhaustive arithmetics, one can verify that $u^* = (u_1^*, u_2^*)$ satisfies the closed-form necessary and sufficient optimality condition $Ae^{A^T u^* - \mathbf{1}} = b$, compare also (16). Note that the set

$$\mathcal{F}_+ = \left\{ t \begin{pmatrix} 1 & 0 & 0 \end{pmatrix}^T + (1-t) \begin{pmatrix} 0 & \frac{2}{3} & \frac{2}{3} \end{pmatrix}^T \mid t \in (0,1) \right\}, \tag{19}$$

is nonempty, compare Fig. 3(b). Exploiting (16), we can compute the maximum energy solution

$$x_E^* = e^{A^T u^* - \mathbf{1}} \approx (0.405918, 0.396055, 0.396055)^T \ .$$

We consider also a slight modification of the previous example. While the discretization and particle position remain the same, we change only the camera positions. This second case considered is schematically represented in Fig. 4(a). The projection matrix and its pseudoinverse are

$$A = \begin{pmatrix} 1 & \frac{1}{2} & 1 \\ \frac{1}{2} & 1 & 1 \end{pmatrix} \quad \text{and} \quad A^+ = \begin{pmatrix} \frac{20}{17} & -\frac{14}{17} & \frac{4}{17} \\ -\frac{14}{17} & \frac{20}{17} & \frac{4}{17} \end{pmatrix}^T$$

and the measurement vector $b = (1, \frac{1}{2})^T$.

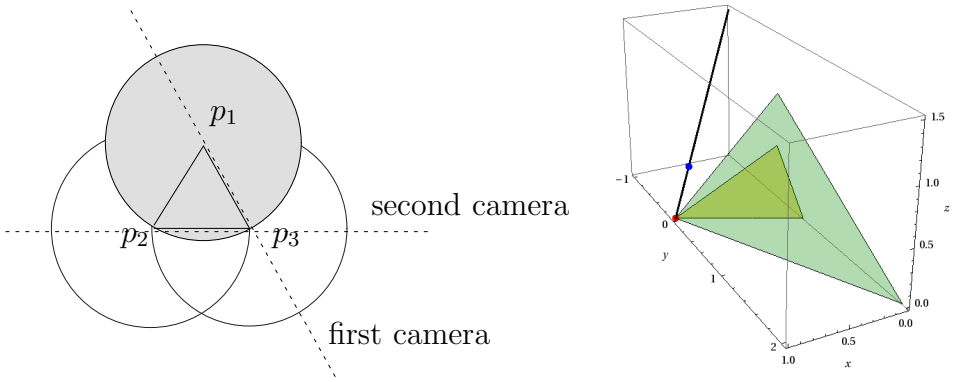

(a) Second case (b) Second case

Figure 4. (a) Discretization of a particle image and corresponding ray geometry. (b) Measurement hyperplanes, single point feasible set w.r.t positivity constraints, sparsest = maximal entropy solution (bottom) and minimal ℓ_2-norm solution (top).

The minimum energy solution x^*_{LS} doesn't belong to the nonnegative orthant in this case. Exact computation yield

$$x^*_{LS} = A^+ b =\approx (0.764705, -0.235294, 0.352941)^T \ .$$

In this second case, the feasible set involving the positivity constraints reduces to a single point, see Fig. 4(b), namely the original solution $x^*_{orig} = (1, 0, 0)^T$. Note that the relative interior of $\mathcal{F}$ is 0 and $\mathcal{F}_+$ is empty.

We tested ART and MART numerically without relaxation, i.e. $\forall k = 1, 2, \ldots, \lambda_k = 1, \mu_k = 1$, on the above examples. Besides ART and MART we consider also a modification of ART, which we further call *ART+pos*, based on constraining strategies proposed in [18]. This method amounts to project the current iterate on the positive orthant after each complete sweep of the ART, through all equations.

We terminate the iteration of the these three algorithms if the condition $\|Ax^k - b\|_2 < 10^{-6}$ is satisfied at the current iterate x^k. The results are summarized in Table 1.

Table 1: Numerical results for the two small-sized experiments detailed in the text

Example	Method	Nr. Iter.	Final iterate value
first	ART	100	$x^f_{LS} = (0.4705884, 0.352942, 0.352940)^T$
	ART+pos	100	$x^f_{LS+} = (0.470588, 0.352942, 0.352940)^T$

	MART	96	$x_E^f = (0.405918, 0.396055, 0.396053)^T$
second	ART	111	$x_{LS}^f = (0.764705, -0.235293, 0.352941)^T$
	ART+pos	382	$x_{LS+}^f = (0.999997, -0.000000, 0.000001)^T$
	MART	1997523	$x_E^f = (0.999998, 0.000000, 0.000001)^T$

We stress that within the first setting MART converged after 96 inner iterations, within the tolerance level, to the positive maximum entropy solution x_E^*. In the second case MART took 1997523 inner iterations for convergence towards $x_{orig}^* = (1, 0, 0)^T$, which is also the sparsest possible in both cases.

As next step we turn our attention to particle image reconstruction based on the Gaussian-blobs discretization. For the purpose of visualization we consider only an example of reduced dimensionality: We consider 40 and 50 particles in a 2D volume $V = [-\frac{1}{2}, \frac{1}{2}] \times [-\frac{1}{2}, \frac{1}{2}]$. The grid refinement was chosen $d = 0.0154$, resulting in 4356 gridpoints. At these gridpoint we centre a Gaussian-type basis function, where $\sigma = d$. Particle positions were chosen randomly but at grid positions, to avoid discretization errors. Four 50−pixel cameras are positioned as depicted in Fig. 6, resulting in a fan beam geometry. The obtained projection matrix, after removing zero rows, is depicted in Fig. 6 (right) and we have $A \in \mathbb{R}^{172\times4356}$. The pixel intensities are computed according to (3), integrating the particle image exactly along each line of sight.

In all three cases we reduce system $Ax = b$ according to the methodology proposed in Proposition 1, see Table 2 for the reduced dimensionalities. We terminate the iteration of the main algorithm if the condition $\|Ax^{k+1} - b\|_\infty < 10^{-4}$ is satisfied or if the maximum iteration number is reached, i.e. $k \geq k_{max}$, where $k_{max} = 1000m_r$, i.e. 1000 complete sweeps through the rows of the reduced matrix A. The relaxation parameters λ_k and μ_k are set to 1.

Table 2: Numerical results for the Gaussian-type discretization examples

#Particles	Method	#Iter.	$m_r \times n_r$	$\|x_{orig} - x^f\|_2$	$\|Ax^f - b\|_\infty$
40	MART	142000	142×3352	5.7078	0.0024
40	ART	142000	142×3352	6.0252	0.0031
40	ART+pos	142000	142×3352	68.6018	0.0059
50	MART	150000	150×4081	6.2935	0.0081
50	ART	150000	150×4081	6.9094	0.0007
50	ART+pos	150000	150×4081	6.5886	0.0161

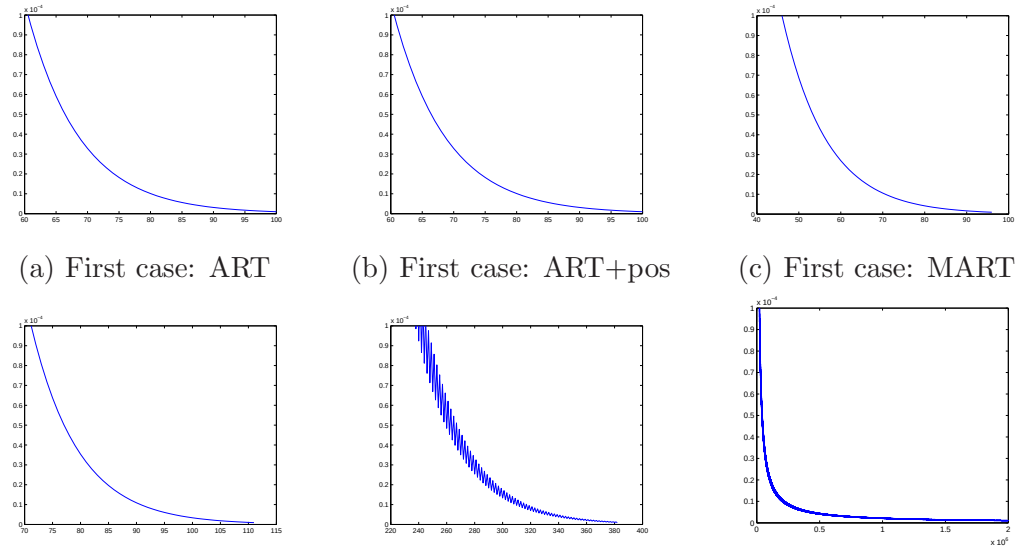

(a) First case: ART (b) First case: ART+pos (c) First case: MART

(d) Second case: ART (e) Second case: ART+pos (f) Second case: MART

Figure 5. Evolution of the ℓ_2-norm error for ART, ART+pos and MART, for the two experiments detailed in the text. Within the first setting the algorithms behave similarly. Here, ART and ART+pos generate identical sequences. The oscillatory behavior in (e) is due to the projection on $\mathbb{R}^3_+$ at every second iteration. (f) MART is substantially slowing down with the loss of the nonempty relative interior assumption.

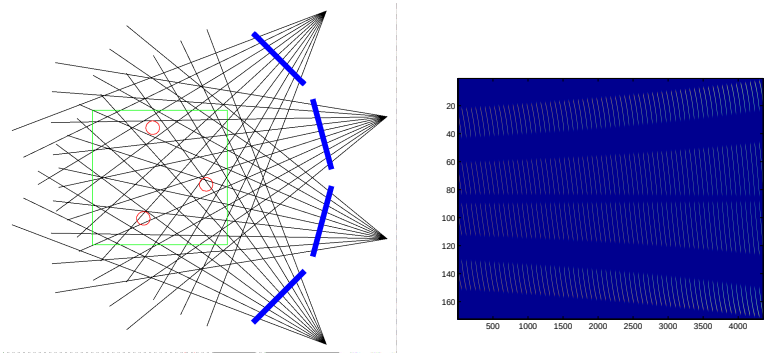

Figure 6. Four cameras measuring the 2D volume from angles $45^o, 15^o, -15^o, -45^o$ (left). Resulting projection matrix (after zero-rows elimination) with about 9% nonzero entries (right)

In Table 2, the first column gives the number of the particles randomly chosen at the $66\times66-$gridpoints; Method gives the name of the algorithm used; Nr. Iter. denotes the total number of inner iterations; $\|x_{orig} - x^f\|_2$ denotes the Euclidean distance of the final iterate x^f from the original particle image x_{orig}, while $\|Ax^f - b\|_\infty$ amounts to a feasibility test at the final iterate.

More significant are the reconstructed particle images, depicted in Fig. 7. The "smearing" of the particles in the lines of the projections is typical for minimum energy reconstructions. This phenomenon is preserved by ART. The MART and ART+pos reconstructions show more distinct particles. However, additional spots are visible, termed as *ghost particles* by the TomoPIV community.

Note that between the reconstructed images via ART, MART etc., the original image seem to be the sparsest of all, i.e. with less non-zero intensities. In view of this observation, sparsity maximization seem to be an adequate optimization approach. We present some preliminary results obtained by a *sequential linearization algorithm (SLA)* [21], especially designed to find the sparsest solution. However, the computational costs are considerably higher. A more detailed motivation for sparsity maximization, along with results obtained via SLA will be reported elsewhere. However, we stress that in all considered examples SLA was able to reconstruct the original image.

7 Conclusion and Further Work

This work focused on tomographic image reconstruction in experimental fluid mechanics (TomoPIV), a recently established research direction. A classical algebraic reconstruction approach that is currently in use, together with closely related variants, were re-considered in some detail to reveal pros and cons from the perspective of TomoPIV. Specifically, we argued that routinely using MART ignores some basic problem characteristics. Promising research directions were outlined to take better into account the needs of the overall objective, the estimation of turbulent flows from accurately reconstructed volume functions.

References

[1] Adrian, R.J., *Twenty years of particle image velocimetry*, Exp. Fluids, **39**(2005), 159–169.

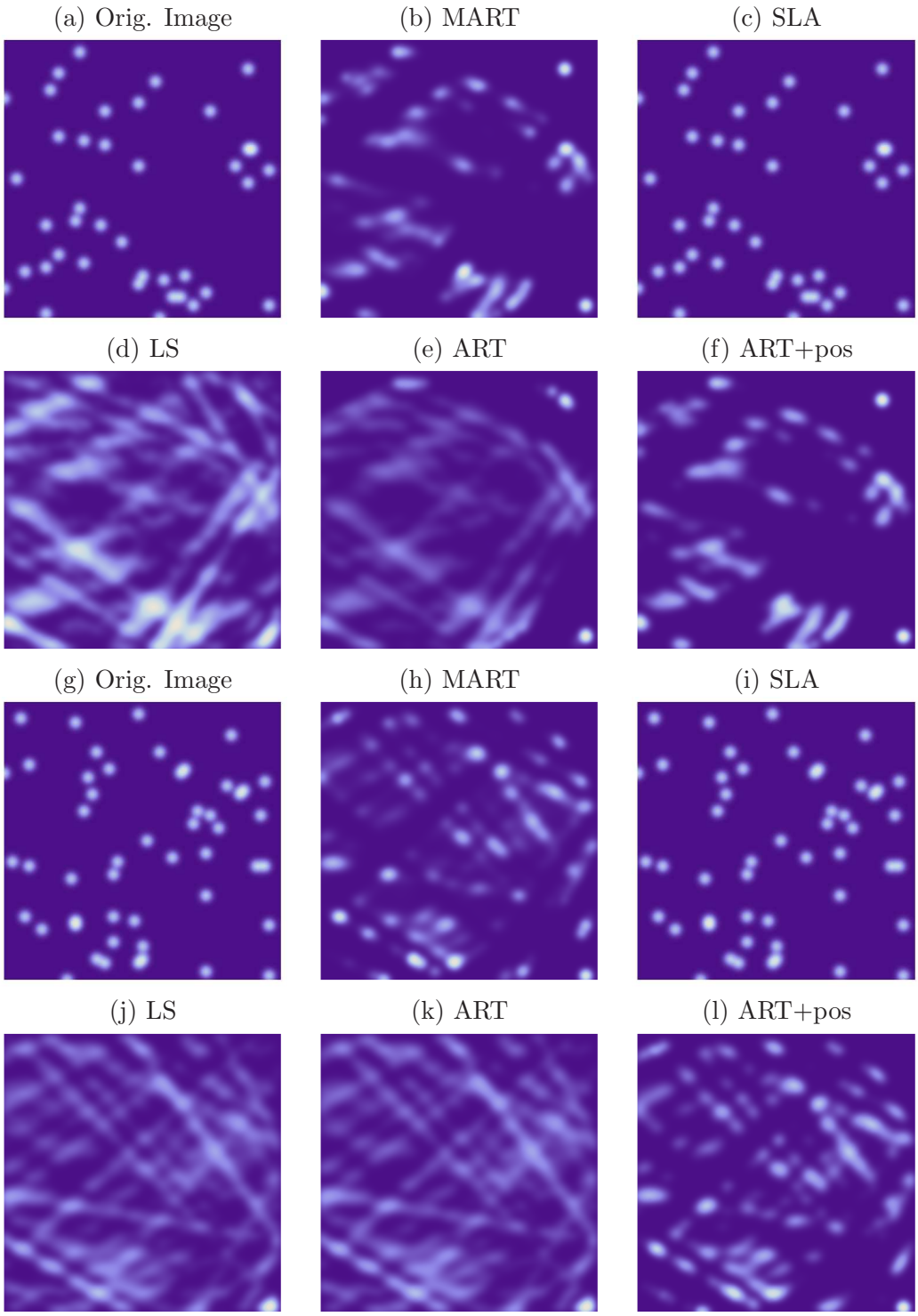

Figure 7. **Top:** (a)-(f) 40 particles and their reconstruction. **Bottom:** (g)-(l) 50 particles and their reconstruction. (a),(g) The original particle distribution contains 40 resp. 50 particles. (b),(h) Reconstruction using MART. (c),(i) Reconstruction using SLA. (d),(j) Minimal norm solution of (P_{LS}) obtained via the Moore-Penrose pseudoinverse A^+, without reducing A. (e),(k) Reconstruction using ART. (f),(l) Reconstruction using ART+pos.

[2] Bauschke, H.H. and Borwein, J.M., *On projection algorithms for solving convex feasibility problems*, SIAM Review, **38**(1996), 367–426.

[3] Bertsekas, D.P., *Nonlinear Programming*, Athena Scientific, 1999.

[4] Bregman, L.M., *The method of successive projections for finding a common point of convex sets*, Soviet Mathematics Doklady, **6**(1965), 688–692.

[5] Brücker, C., *it Digital Particle Image Velocimetry (DPIV) in a scanning light-sheet: 3D starting flow around a short cylinder*, Exp. Fluids, **19**(1995), 255–263.

[6] Censor, Y., Eggermont, P. and Gordon, D., *Strong underrelaxation in Kaczmarz method for inconsistent systems*, Numer. Math., **41**(1983), 83–92.

[7] Censor, Y. and Zenios, S.A., *Parallel Optimization: Theory, Algorithms and Applications*, Oxford University Press, New York, 1997.

[8] Cover, T.M. and Thomas, J.A., *Elements of Information Theory*, John Wiley & Sons, Inc., New York, 1991.

[9] Elad, M., Bruckstein, A.M. and Zibulevsky, M., *A Non-Negative and Sparse Enough Solution of an Underdetermined Linear System of Equations is Unique*, IEEE Trans. Inf. Theory, **54**(2008), 4813–4820.

[10] Elfving, T., *On some methods for entropy maximization and matrix scaling*, Linear Algebra Appl., **34**(1980), 321–338.

[11] Elsinga, G., Scarano, F., Wieneke, B. and van Oudheusden, B., *Tomographic particle image velocimetry*, Exp. Fluids, **41**(2006), 933–947.

[12] Fang, S.C., Rajasekera, J.R. and Tsao. H.S.J., *Entropy Optimization and Mathematical Programming*, Kluwer Academic Publishers, Boston, 1997.

[13] Gordon, R., Bender, R. and Herman G.T., *Algebraic reconstruction techniques (ART) for three-dimensional electron microscopy and X-ray photography*, J. Theor. Biol. **29**(1970), 471–481.

[14] Gubin, L., Polyak, B. and Raik, E., *The method of projections for finding the common point of convex sets*, USSR Comp. Math. Math+., **7**(1967), 1–24.

[15] Hinsch, K.D., *Holographic particle image velocimetry*, Meas. Sci. Technol., **13**(2002), 61–72.

[16] Herman, G., Lent, A., and Lutz, P., *Relaxation methods for image reconstruction*, Commun. Assoc. Comput. Mach., **21**(1978), 152–158.

[17] Kaczmarz, S., *Angenäherte Auflösung von Systemen linearer Gleichungen*, Bull. Acad. Polonaise Sci. et Lettres **A**(1937), 355–357.

[18] Koltracht, I. and Lancaster, P., *Contraining Strategies for Linear Iterative Processes*, IMA J. Numer. Anal. **10**(1990), 55–567.

[19] Lent, A. and Censor. Y., *The primal-dual algorithm as a constraint-set-manipulation device*, Math. Program., **50**(1991), 343–357.

[20] Maas, H.-G., Grün, A. and Papantoniou, D., *Particle Tracking in three-dimensional turbulent flows*, Exp. Fluids, **15**(1993), 133–146.

[21] Mangasarian, O.L., *Minimum-support solutions of polyhedral concave programs*, Optimization, **45**(1999), 149–162.

[22] Popa, C., *Extensions of block-projections methods with relaxation parameters to inconsistent and rank-deficient least-squares problems*, BIT, **38**(1998), 151–176.

[23] Popa, C. and Zdunek, R., *Kaczmarz extended algorithm for tomographic image reconstruction from limited-data*, Math. Comput. Simulat., **65**(2004), 579–598.

[24] Raffel, M., Willert, C. and Kompenhans, J., *Particle Image Velocimetry*, 2nd edition, Springer, 2001.

[25] Scarano, F. and Riethmüller, M.L., *Advances in iterative multigrid PIV image proccesing*, Exp. Fluids, **29**(2000), 51–60.

[26] Tanabe, K., *Projection Method for Solving a Singular System of Linear Equations and its Applications*, Numer. Math., **17**(1971), 203 – 214.